Solar/Radiative Cooling Dual-Regulation Smart Window Based on Shape-morphing Kirigami Structures

Shancheng Wang,[a,b‡] Yuting Dong, [b,‡] Yanbin Li,[c,‡] Keunhyuk Ryu,[b] Zhili Dong,[b] Jian Chen,[d] Zhendong Dai,[d] Yujie Ke,[e,*] Jie Yin,[c,*] and Yi Long[a,b,*]

[a]Department of Electrical Engineering, The Chinese University of Hong Kong, Shatin, New Territories, Hong Kong SAR, China

[b]School of Materials Science and Engineering, Nanyang Technological University, 639798 Singapore

[c]Department of Mechanical and Aerospace Engineering, North Carolina State University, Raleigh, North Carolina 27695, United States

[d]Jiangsu Provincial Key Laboratory of Bionic Functional Materials, College of Mechanical and Electrical Engineering, Nanjing University of Aeronautics and Astronautics, Nanjing 210016, China

[e]Institute of Materials Research and Engineering (IMRE), Agency for Science, Technology and Research (A*STAR), 2 Fusionopolis Way, Innovis #08-03, Singapore 138634, Republic of Singapore

[‡]These authors contributed equally to this work.

Email: yilong@cuhk.edu.hk; jyin8@ncsu.edu; yujie_ke@imre.a-star.edu.sg

Abstract

Building energy efficiency arouses a critical concern due to its substantial contribution to global energy consumption. Windows, in particular, are often the least efficient component of the building envelope, and conventional smart windows focus solely on regulating solar transmittance while overlooking radiative cooling. Although several recent designs achieved dual-control of solar and radiative cooling, these windows still face limitations in terms of durability, limited modulation ability and energy-saving performance. To address these challenges, we propose a novel dual-control smart window design that consists of a reconfigurable kirigami structure and polydimethylsiloxane-laminated thermochromic hydrogel with silver nanowires overcoating. In summer, the thermochromic hydrogel turns translucent to suppress the solar heat gain, while the high emissivity kirigami structure covers

the exterior surface of the window to prompt radiative cooling. In winter, the hydrogel becomes transparent to allow for solar transmission. And the kirigami structure undergoes an out-of-plane structural change opening towards the outside environment to expose the underlying low-emissivity silver nanowires and suppress heat radiation. Our design achieves a promising solar transmittance modulation ability of ~24% and a good long-wave infrared emissivity regulation ability of 0.5. Furthermore, it exhibits significantly improved durability that is nine times longer than the lifespan of conventional smart hydrogels. Our novel approach offers a promising solution for constructing energy-efficient and durable smart windows, and outperforms existing state-of-the-art Solar/Radiative Cooling Dual-Regulation Smart Window in the literature.

Introduction

Buildings are responsible for approximately half of the global electricity supply,[1] and windows are among the least energy-efficient components of building envelopes.[2, 3] In the United States, window-associated heating and cooling energy consumes about 4% of the national primary energy usage.[4] To address this issue, researchers have developed several types of chromogenic smart windows such as electro-,[5, 6] thermo-,[7, 8] photo-,[9, 10] and mechano-chromic windows[11, 12] to improve the energy efficiency of windows by regulating the visible (360-780 nm) and near-infrared (NIR, 780-2500 nm) transmittance. Although these types of chromogenic smart windows have shown promise in improving energy efficiency, they can only regulate solar radiation while generally overlooking the broadband infrared emissivity ($\varepsilon_{\text{Broadband,}}$ 2.5-25 μm) and its accompanied radiative cooling (RC) effect.. RC is a technique that spontaneously cools an object through strong sky-towards outgoing thermal radiation and minimum solar radiation absorption.[13, 14] Recent literature demonstrated that ideal energy-efficient smart window should have low solar transmittance (T_{sol}, 250-2500 nm) and high $\varepsilon_{\text{Broadband}}$ in summer to minimize the solar radiation absorption and maximize the RC, respectively; while the window in winter should have high T_{sol} to prompt solar heating and low $\varepsilon_{\text{Broadband}}$ to suppress the RC.[15]

Based on the afore mentioned state-of-the-art design principle, several dual-control smart windows have been developed recently by employing thermal-responsive material to construct optical modulation structures,[15, 16] thermal-responsive water capture/release in hydrogel,[17] reversible electrodeposition of metal,[18] reversible crack creation on low-E film,[19] and mechanical flipping between high-/low-E faces.[20] These designs can spontaneously control the solar transmittance while regulating the RC power. Consequently, these dual-control smart

windows offer significantly improved energy efficiency compared to conventional smart windows, particularly in four-seasoned regions.

Despite the promise of these dual-control smart window designs, they still face limitations in terms of durability and modulation capability. For example, the thermal-responsive vanadium dioxide (VO_2) is prone to oxidation.[21, 22] While the current remedies such as sealing[23, 24] and encapsulation,[25] can improve the durability of VO_2 while at the cost of defunctionalizingVO_2's $\varepsilon_{Broadband}$ modulation ability. Stimuli-responsive hydrogels and reversible metal electrodeposition also suffer from durability issues due to the factors such as vulnerability to drying[26, 27] and electrochemical cell performance degradation.[28, 29] Meanwhile, the reversible crack creation approach has limited RC regulating performance,[19] and the facile mechanical flipping technique requires specially designed pivoted window frames and manual operation for achieving high regulating performances.[20] Therefore, a solar/RC dual-control smart window is highly desired with both good durability and promising solar/RC regulating performance.

To address these issues, we have developed a new design of a kirigami-inspired durable solar/RC dual-control smart window by integrating thermal-responsive hydrogels with an out-of-plane reconfigurable kirigami structure. As shown in Figure 1a and 1b, the design consists of two components: (1) an AgNWs coated, polydimethylsiloxane (PDMS) laminated thermal-responsive composite hydrogels based on physical-crosslinked poly(N-isopropylacrylamide) (PNIPAm) and acrylamide, and (2) a PDMS-based kirigami structure with strain-responsive out-of-plane opening for emissivity tuning. Its working principles in summer and winter are illustrated in Figure 1c and 1d, respectively. In summer, the high-E PDMS kirigami is in the released state to cover the entire exterior surface of the window to enhance RC, while the hydrogel composite becomes translucent to suppress solar transmission as the ambient temperature above its lower critical solution temperature (LCST, 20 °C for thermal-responsive composite hydrogel). In winter, the kirigami structure undergoes out-of-plane structural change and opens towards the outside environment to expose the underlying low-E AgNWs layer to suppress RC, while the smart hydrogel becomes transparent to allow for solar transmission and heating. The transparent-to-translucent transition of the hydrogel is based on a phase separation process due to the hydrophobic-to-hydrophilic changes of the PINIPAm polymer across its LCST.[30, 31] The newly designed smart window shows nine times lifetime extension compared with conventional smart hydrogels, and it exhibits a promising $\varepsilon_{Broadband}$ regulation ability ($\Delta\varepsilon_{Broadband}$) of 0.5 ($\varepsilon_{Broadband, Release}$: 0.95, $\varepsilon_{Broadband, Stretch}$: 0.45). Due to its balanced luminous

transmittance (T_{lum}, 360-780 nm), solar modulation ability (ΔT_{sol}, 250-2500 nm), and $\Delta\varepsilon_{Broadband}$, the new design outperforms the literature-reported designs of state-of-the-art Solar/Radiative Cooling Dual-Regulation Smart Windows regarding the global energy-saving performance. Our new design of the durable solar/RC dual-control smart window provides a new strategy to pave the way for the applications in real scenarios.

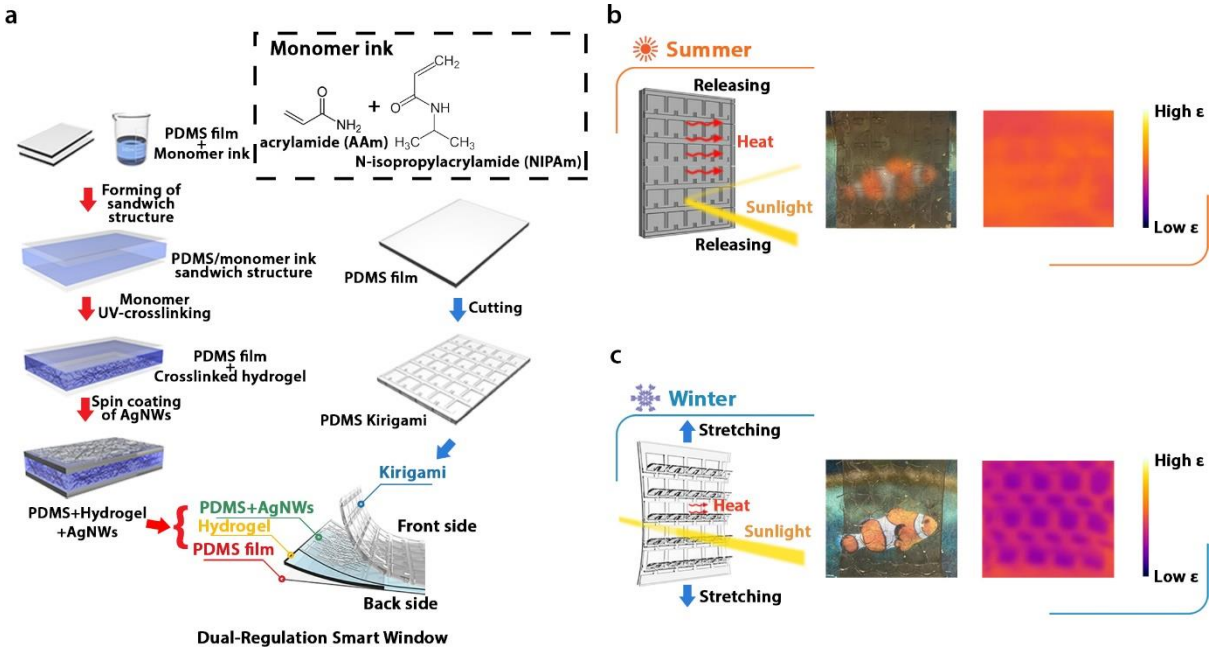

Figure 1. a) Formula of acrylamide and N-isopropylacrylamide monomers used in smart monomer ink. And schematics of the fabrication process and structure of the durable solar/RC dual-control smart window. b) Working principle of durable solar/RC dual-control smart window in summer, and its corresponding photo and IR camera image. The red arrows represent thermal radiation, and the yellow line represents sunlight. In summer, the high-E kirigami overlayer closes to promote thermal radiation, and the hydrogel turns translucent to block the sunlight. c) Working principle of durable solar/RC dual-control smart window in winter, and its corresponding photo and IR camera image. In winter, the kirigami overlayer opens towards outside environment under an in-plane stretching, which allows the sunlight enters the room to suppress the RC to minimize heat loss.

Characterization of PNIPAm-based hydrogel and AgNWs coating.

As the PNIPAm is the active ingredient to fulfil the functionality of solar transmittance regulation in the hydrogel composite, we investigated the thermochromic property changes in terms of PNIPAm concentration in hydrogel composite (figure S1, table S1) and summarized them in Figure 2a. All hydrogel composites show a similar $T_{lum,15°C}$ of ~90%, irrespective of their PNIPAm concentration. While their ΔT_{sol} increases with increasing PNIPAm concentration from 5wt% to 10wt% and reaches a plateau at approximately 60% for samples

with PNIPAm concentration above 10wt%. All smart hydrogel samples experience hydrophobic-to-hydrophilic phase transitions in response to a thermal stimulus and show an LCST of 20 °C (figure S2), which is significantly lower than the pure PNIPAm of 30 °C.[32] Additionally, the viscosity of the monomer ink increased with increasing NIPAm concentration (5wt% PNIPAm sample: 115.8 cP; 20wt% PNIPAm sample: 2650.6 cP), and the monomer ink successfully crosslinks to form hydrogels under UV irradiation has been proven by storage modulus (G') and loss modulus (G") changes (figure S3). Meanwhile, figure S4 illustrates the stress-strain curve of crosslinked hydrogel with different PNIPAm concentrations. It can be observed that when the PNIPAm concentration increases from 5wt% to 20wt%, Young's modulus of hydrogel decreases from 38.08±0.35 kPa to 24.64±0.25 kPa. To balance the thermochromic properties fabrication quality, and mechanical property the hydrogel with 10wt% PNIPAm was chosen for the application in the durable solar/RC dual-control smart window. Figure 2b shows the UV-Vis-NIR spectra for composite hydrogels with 10wt% PNIPAm at 15 °C and 45 °C. The 1-mm thick hydrogel sample has a T_{lum} of 88.8% and a ΔT_{sol} of 60.5%, with a transparency appearance at 15°C and a translucent appearance at 45°C (Figure 2c). The photos of hydrogel composites with different PNIPAm concentrations are shown in figure S5. The light regulation behaviour of the PNIPAm-based hydrogel composite is attributed to the porous polymer networks as demonstrated by the scanning electron microscope (SEM) images. At low temperatures, the size of pores is large to allow the light to pass through. In contrast, the pores shrink when heated and serve as the scattering centre, resulting in a decrease in transmittance.

Meanwhile, we tested and calculated the T_{lum}, T_{sol}, and $\varepsilon_{Broadband}$ for the PDMS films with different layers of AgNWs coating (Figure 2d, figure S6, S7, table S2). The transparency of the PDMS films with varying layers of AgNWs coating is shown in figure S8, and the $\varepsilon_{Broadband}$ of the coated PDMS films decreases from 0.70 to 0.16 with increasing coating layers from 1 to 15, which is consistent with their IR photos (figure S9). The T_{lum} and T_{sol} follow a similar trend to the $\varepsilon_{Broadband}$. Since $\Delta\varepsilon_{Broadband}$ is crucial for energy saving, an optimal 15-layer AgNWs coating on PDMS film was chosen for the application in the durable solar/RC dual-control smart window. The $\varepsilon_{Broadband}$ of the stretched AgNWs coated PDMS is lower (0.16) than that of the released state (0.34) throughout the wavelength of 2.5-20 μm, as shown in Figure 2e. This behaviour can be attributed to the surface roughness change induced by the stretch/release of the PDMS substrate (Figure 2f). As the PDMS substrate is pre-stretched to 40% strain during the spin coating process, the AgNWs layers become wrinkled in the released state, leading to

increased surface roughness and consequently an increase in $\varepsilon_{Broadband}$. In contrary, the surface of the AgNWs layer is smooth in the 40% stretched state, rendering a lowered $\varepsilon_{Broadband}$.

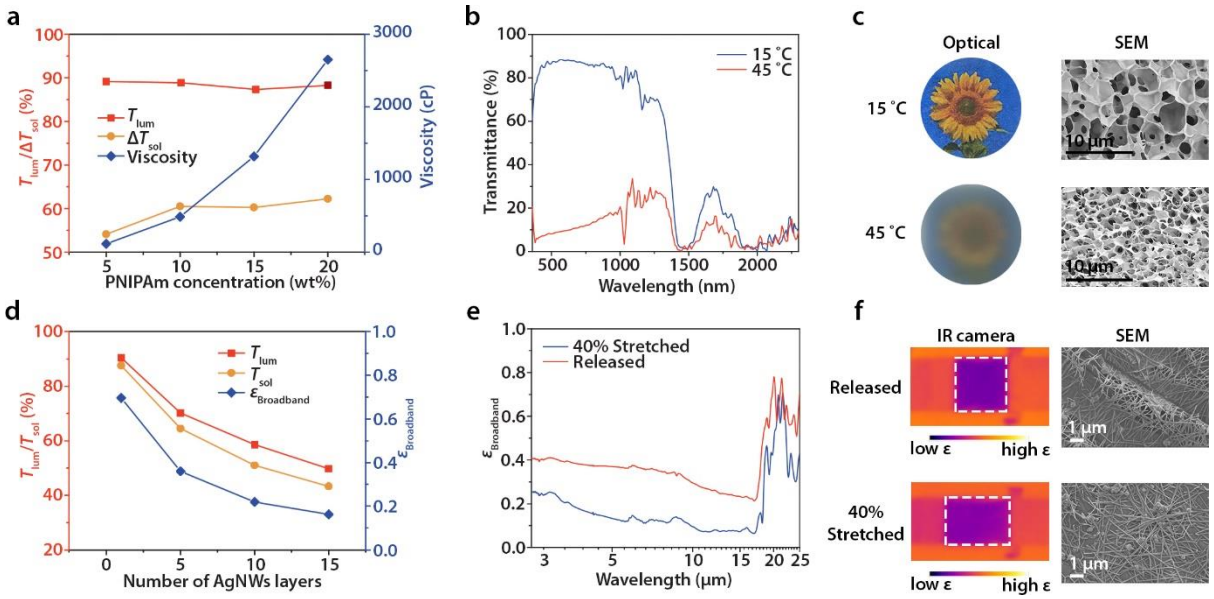

Figure 2. a) Thermochromic properties for hydrogel composite and viscosity of monomer ink with different PNIPAm concentrations. b) UV-Vis-NIR spectra for 10wt% PNIPAm hydrogel at 15 °C and 45 °C. c) Photo and SEM image of the smart hydrogel at 15 and 45 °C. d) The T_{lum}, T_{sol}, and integrated $\varepsilon_{Broadband}$ for PDMS film with different layers of AgNWs coating. e) Broadband emissivity spectra of the 15-layer AgNWs-coated PDMS film in its released and 40%-stretched states. f) IR camera images and SEM images for 15-layer AgNWs-coated PDMS film in its released and 40%-stretched states.

Designing of kirigami-inspired out-of-plane shape-morphing structures

Different from the reported cutting manners for kirigami structures that commonly produce in-plane structural changes,[33, 34] we adapted a kirigami pattern to achieve out-of-plane reconfigurable structural changes[35] and investigated its behaviour with different feature parameters. The geometric designs of the kirigami patterns and their feature parameters are displayed in the upper part of Figure 3a and figure S10, respectively. We defined the asymmetric cut ratio as the height ratio between the upper patterns (labelled as H_1 in Figure 3a) and lower patterns (labelled as H_2 in Figure 3a). The photos of paper kirigami structures with different asymmetric cut ratios are illustrated in the middle part of Figure 3a. Under the 40%-stretching state, the sample with an asymmetric ratio of 1 deforms and opens symmetrically on two sides out of the original plane (highlighted with the red dashed line in Figure 3a). Conversely, the sample with a ratio of 3 opens asymmetrically towards one side only. Similar

structural change behaviour was observed on PDMS kirigami structures (Figure 3a lower part, figure S11).

To quantitatively understand the asymmetrical reconfiguration behaviour of the kirigami structure, we defined two performance indices, namely, length ratio and covering ratio (Figure 3b, upper part). Finite element method simulations (FEM) were conducted for the samples with various asymmetric ratios, and the results are presented in Figure 3b (middle part). Both simulation and experiment results suggest that the length ratio increases linearly with the increasing asymmetric ratio (Figure 3b, lower part): *i.e.*, kirigami structures with higher asymmetric ratios tend to open towards one side upon stretching, with a smaller portion at the other side of the original plane. The one-side opening will minimize the squeezing and scratching of the underlying AgNWs layer during the kirigami structural reconfiguration, and extend the lifetime of AgNWs. On the other hand, the change in covering ratio is insignificant regarding the asymmetric ratio changing, indicating that the change of opening directions will not affect the exposure degree of the underlying AgNWs layer and its maximum $\varepsilon_{\text{Broadband}}$ regulation ability. The working principle for the directional opening is further investigated by FEM simulations (figure S12, video S1 to S5). The models with different asymmetric ratios from 1 to 10 were stretched, and all the structures buckle out of the stretching plane and overlap with a pivot axis at the centre of two adjacent cut slits (figure S13). Meanwhile, the stress distributions in the kirigami structures with different asymmetric ratios are mapped (figure S14). The maximum value of the concentrated stress in the kirigami structure is ~0.00186 MPa, which is significantly lower than the rupture stress threshold of PDMS materials (~0.83 MPa).

In the design of kirigami for smart window applications, strength and stiffness are critical factors. The ideal kirigami structure for smart window application should be responsive to small amounts of tensile stress, which means that it should have low tensile strength and stiffness. We prepared kirigami structures with different PDMS thicknesses (figure S15) and tested their tensile strength and stiffness. Figure 3c shows the stress-strain curves of kirigami structures with different PDMS thicknesses from 0.3 to 0.6 mm. With the film thickness increasing, the kirigami structures show an increased Young's modulus and toughness (Figure 3d). The opening angle is also affected by the thickness: the 0.3-mm sample exhibits an open angle of 75.5° at a stretched strain of 40%, while the 0.6 mm sample only opens to 44.5° (Figure 3e). Therefore, a PDMS film with a thickness of 0.3 mm is preferred for smart window applications due to its relatively low tensile strength and stiffness, as well as the relatively large opening degree upon stretching. It is worth noting that the 0.3-mm PDMS kirigami structure

shows little change in T_{lum} between the released and 40% stretched states (figure S16), which suggests that the out-of-plane structural change process will not affect its optical properties.

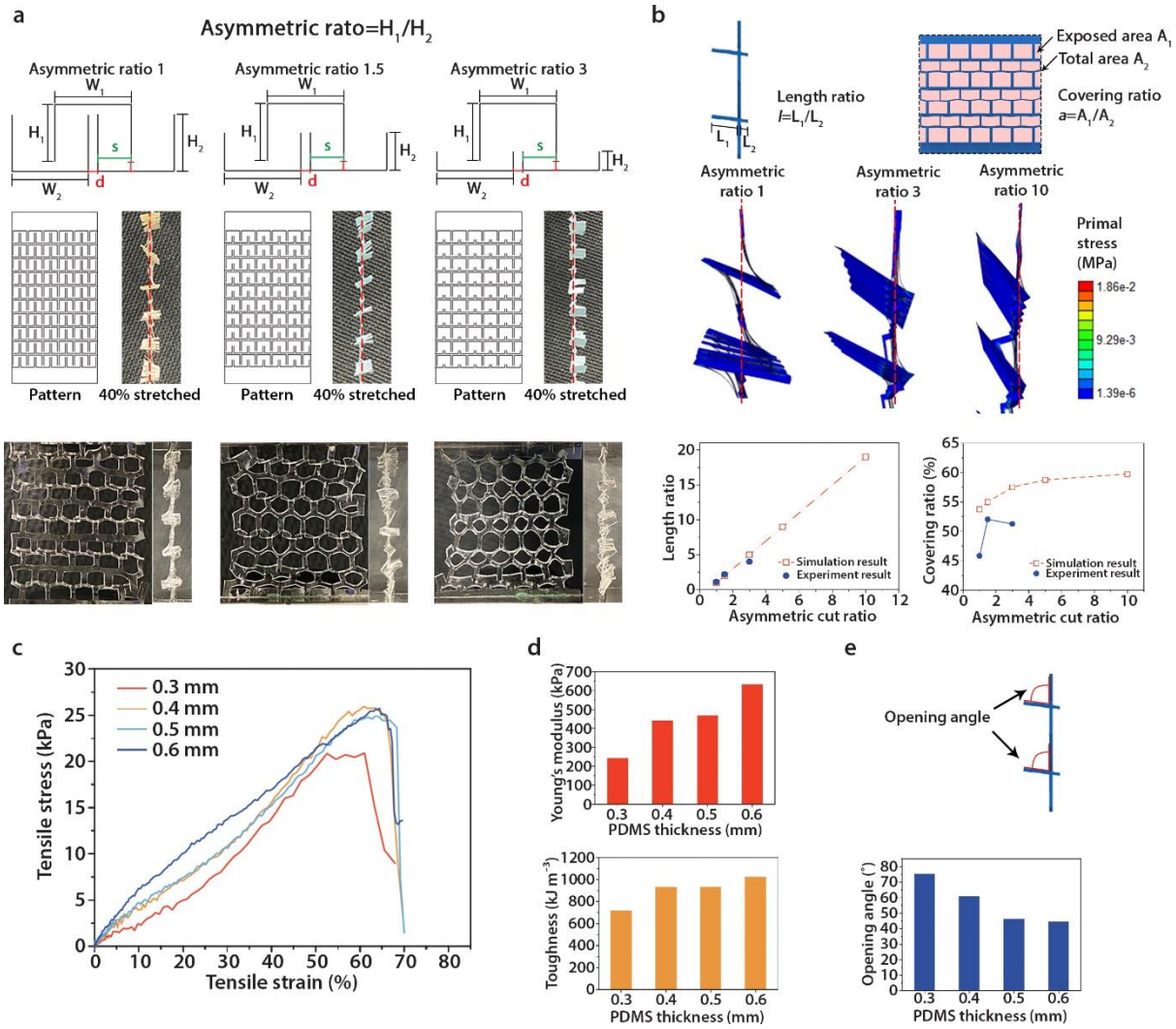

Figure 3. a) Scheme of out-of-plane reconfigurable kirigami pattern with different asymmetric cut ratios (upper part), its corresponding paper kirigami structures under 40% stretching (middle part), and its corresponding PDMS structures under 40% stretching (lower part). The red dashed line indicates their original plane in the released state. b) Numerical analysis for the out-of-plane structural changes of kirigami structures. Upper part: Schemes of the indexes to describe the out-of-plane structural changes: the length ratio and the covering ratio. Middle part: Simulated model for asymmetric ratio 1, 3, and 10 samples. Lower part: Experimental (solid dots) and simulational (hollow squares and dashed line) results for length ratio and covering ratio of samples with different asymmetric ratios. c) Stress-strain curves for the kirigami structures with different PDMS film thicknesses. d) Effect of the PDMS thickness on Young's modulus and toughness. e) Scheme of opening angle and the experimental angle analysis for samples with different PDMS thicknesses under 40% stretching.

Performance evaluation of durable solar/RC dual-control smart window

We further evaluated the performance of the fabricated durable solar/RC dual-control smart window. Figure 4a shows the UV-Vis-NIR spectra of the smart window at 15 °C and 45 °C, respectively. The smart window has lower T_{lum} and ΔT_{sol} than the smart hydrogels (T_{lum}: 37.1% vs. 88.8%; ΔT_{sol}: 23.7% vs. 60.5%), which is due to AgNW-induced strong reflection in visible and NIR regions (figure S17). Notably, the T_{lum} of 37.1% meets the building energy standard of the American Society of Heating, Refrigerating, and Air-Conditioning Engineers (ASHRAE), which recommends an assembly maximum solar heat gain coefficient of 0.21 to 0.40 for climate zones 1 to 7.[36] Figure 4b illustrates the photo of 5cm×5cm durable solar/RC dual-control smart window sample at different temperatures from 15 to 45 °C, and the sample gradually changes from transparent to translucent. The $\varepsilon_{Broadband}$ spectra of the smart window at 40% stretched and released states are shown in Figure 4c. In the released state, the sample has a high $\varepsilon_{Broadband}$ of 0.95 since its surface is fully covered by the high-E PDMS. In the 40%-stretched state, the out-of-plane structural deformation of the kirigami structure partially opens and exposes the low-E AgNWs layer underneath, resulting in a significantly decreased $\varepsilon_{Broadband}$ of 0.45. Figure 4d demonstrates the switching process of $\varepsilon_{Broadband}$ via an IR camera, where the sample shows a gradual change from orange (high $\varepsilon_{Broadband}$) to blue (low $\varepsilon_{Broadband}$) upon stretching.

The ageing test was conducted to assess the durability of the smart window. The PNIPAm hydrogel control sample and PDMS laminated hydrogel were subjected to durability evaluation in an environment of 25 °C and humidity of 10%RH. Figure 4e shows their change of transmittance at 650 nm (ΔT_{650nm}) with an increasing exposing time. It is observed that the control sample lost its optical modulation function after 6 h, while the PDMS laminated hydrogel retained its optical modulation ability for approximately 52 h, which is 9 times longer than the control sample. Furthermore, the laminated hydrogel exhibits a lifetime of 4 times longer than that of the conventional smart hydrogel in the high-temperature durability test (figure S18). The durability evaluation results demonstrate that the PDMS lamination can effectively extend the lifetime of smart hydrogel through sealing and preventing water evaporation. We further compare the lifetime of the laminated hydrogel with that reported in the literature (Table 1) and found that it has a longer service time than conventional hydrogel preservation methods, such as forming organohydrogel[37-40] or introducing ionic salt-based water absorbents.[41] Furthermore, it is worth mentioning that the introduction of ionic salt can deactivate the smart function of hydrogels,[42] which is not preferred. The cycle stability test

results of the smart window are presented in figure S19, which demonstrates that the window retains its solar modulation ability within 125 heating-cooling cycles.

Table 1. The lifetime of recently reported long-lifetime hydrogels

Hydrogel name	Temperature (°C)	Humidity (%RH)	Lifetime (h)	Reference
PDMS laminated hydrogel	**25** **60**	**10** **10**	**52** **24**	**This work**
Glycol-poly (SBMA-co-AA) organohydrogel	25	54	9	[37]
Ethylene glycol-PAAm organohydrogel	60	37	10	[38]
PAAm-carrageenan-glycol organohydrogel	25	70	20	[39]
PAM/CA double network hydrogel/organohydrogel	25	50	30	[40]
PAAm-$MgCl_2$ hydrogel	25	10	25	[41]
PAAm-LiCl hydrogel	25	10	40	[41]

The building energy consumption simulation was conducted to evaluate the energy-saving capability of the durable solar/RC dual-control smart window. In this simulation, an apartment model (8 m in length, 6 m in width, and 2.7 m in height) with four windows (3 m in width and 2 m in height) was used (figure S20). The windows were placed on all four sides of the building to avoid orientation bias. To assess the durable solar/RC dual-control smart window's performance, we compared its global average energy-saving performance with two other types of smart windows reported in the literature: passive RC regulating thermochromic (RCRT) smart window,[15] and solar and thermal regulatory thermochromic (STR) smart window (Figure 4f).[17] In this energy-saving performance comparison, clear glass served as the baseline, and table S3 presents the optical data for the clear glass and the durable solar/RC dual-control smart window utilized in the simulation. The comparison of average energy-saving performance shows that the new design has a higher global energy-saving performance (19.2%) compared to the passive stimuli-responsive RCRT window (13.7%) and STR window (8.3%) (Figure 4f). We further compare their performance in Figure 4g regarding the five performance indexes of window namely energy saving, T_{lum}, ΔT_{sol}, transition temperature (τ_c), and $\Delta\varepsilon_{Broadband}$. The

durable solar/RC dual-control smart window exhibits the best energy-saving performances with a good balance of T_{lum}, ΔT_{sol}, τ_c, and $\Delta\varepsilon_{Broadband}$ among the candidates. We further conducted a 24-hour room temperature simulation for the smart window, clear glass, conventional hydrogel, and low-E glass(figure S21). The results reveal that during the summer season, the room with durable solar/RC dual-control smart window exhibits a lower temperature of ~2°C in the daytime compared to the clear glass sample. Conversely, during the winter season in cold regions, the smart window demonstrates a higher room temperature than the other samples throughout the day. Overall, the newly developed durable solar/RC dual-control smart window displays promising energy-saving performance due to its tunable solar transmittance and longwave infrared emissivity.

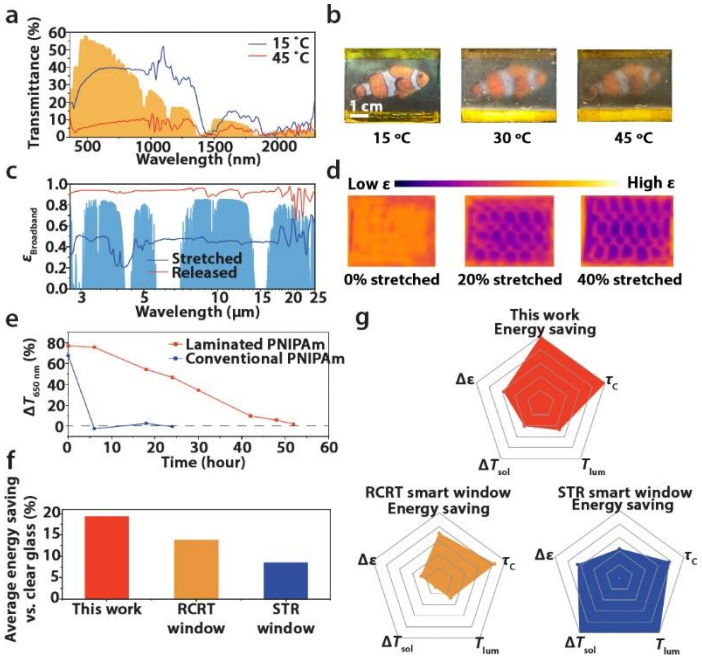

Figure 4. a) UV-Vis-NIR spectra of durable solar/RC dual-control smart window at 15 °C and 45 °C. The orange shadow represents the AM1.5 global spectrum. b) Photos of durable solar/RC dual-control smart window at 15, 30, and 45 °C. c) Broadband emissivity spectra of durable solar/RC dual-control smart window in released and stretched states, d) IR camera images of durable solar/RC dual-control smart window at 0%, 20%, and 40% stretch. e) Durability test result for PNIPAm and PDMS laminated PNIPAm in the 10%RH and 25 °C environment. f) Global average energy saving performance of the durable solar/RC dual-control smart window, RCRT smart window, and STR smart window. g) Performance comparison among durable solar/RC dual-control smart window and the reported RCRT and STR smart windows.

Conclusion

In this study, we presented a new design of kirigami-inspired durable solar transmittance/radiative cooling dual-control smart window by integrating out-of-plane shape-morphing kirigami structures with PDMS laminated thermal-responsive smart hydrogel. Our design has demonstrated significant improvements in durability with a nine-fold increase compared to conventional smart hydrogels such as organohydrogels and ionic salt-soaked hydrogels. By manupilating the geometrical feature, the kirigami structure helps to maintain the mechanical integrity of the underlying low-E layer through out-of-plane structural change, while keeping the promising $\varepsilon_{\text{Broadband}}$ regulation ability. Through balancing T_{lum}, ΔT_{sol}, and $\Delta \varepsilon_{\text{Broadband}}$, the newly designed durable solar/RC dual-control smart window demonstrated better energy-saving performance than the literature-reported RCRT and STR smart windows. Given its enhanced durability and promising energy-saving performance, the new smart window will inspire energy-efficient window design and construction.

Acknowledgement

Y.L. wishes to thank for funding support from the Global STEM Professorship Scheme sponsored by the Government of Hong Kong Special Administrative Region, Start-up funding from The Chinese University of Hong Kong, and Ministry of Education, Singapore under its Tier 1 Grant: RG71/21.

Author contributions

S.Wang: Investigation, Formal Analysis, Visualization, Writing – Original Draft; **Y.Dong**: Investigation, Formal Analysis, Visualization, Writing – Original Draft; **Y.Li**: Investigation, Software, Visualization, Writing – Original Draft; **K.Ryu**: Visualization; **Z.Dong**: Supervision, Writing – Review & Editing; **J.Chen**: Investigation; **Y.Ke**: Validation, Writing – Review & Editing; **Z.Dai**: Supervision, Writing – Review & Editing; **J.Yin:** Supervision, Software, Writing – Review & Editing; **Y.Long**: Conceptualization, Funding Acquisition, Project Administration, Supervision, Writing – Review & Editing.

Reference

1. U. Berardi, *Resources, Conservation and Recycling*, 2017, **123**, 230-241.
2. L. Zhao, X. Lee, R. B. Smith and K. Oleson, *Nature*, 2014, **511**, 216.
3. Y. Gao, S. Wang, L. Kang, Z. Chen, J. Du, X. Liu, H. Luo and M. Kanehira, *Energy Environ. Sci.*, 2012, **5**, 8234-8237.
4. E. S. Lee, X. Pang, S. Hoffmann, H. Goudey and A. Thanachareonkit, *An empirical study of a full-scale polymer thermochromic window and its implications on material science development objectives*, Report 0927-0248, Lawrence Berkeley National Laboratory, 2013.

5. Z. Shao, A. Huang, C. Ming, J. Bell, P. Yu, Y.-Y. Sun, L. Jin, L. Ma, H. Luo, P. Jin and X. Cao, *Nature Electronics*, 2022, **5**, 45-52.
6. R. Li, X. Ma, J. Li, J. Cao, H. Gao, T. Li, X. Zhang, L. Wang, Q. Zhang, G. Wang, C. Hou, Y. Li, T. Palacios, Y. Lin, H. Wang and X. Ling, *Nat. Commun.*, 2021, **12**, 1587.
7. Y. Zhou, S. Wang, J. Peng, Y. Tan, C. Li, F. Y. C. Boey and Y. Long, *Joule*, 2020, **4**, 2458-2474.
8. Q. Zhang, Y. Jiang, L. Chen, W. Chen, J. Li, Y. Cai, C. Ma, W. Xu, Y. Lu, X. Jia and Z. Bao, *Adv. Funct. Mater.*, 2021, **31**, 2100686.
9. A. Kanwat, B. Ghosh, S. E. Ng, P. J. S. Rana, Y. Lekina, T. J. N. Hooper, N. Yantara, M. Kovalev, B. Chaudhary, P. Kajal, B. Febriansyah, Q. Y. Tan, M. Klein, Z. X. Shen, J. W. Ager, S. G. Mhaisalkar and N. Mathews, *ACS Nano*, 2022, **16**, 2942-2952.
10. S. Y. Chun, S. Park, S. I. Lee, H. D. Nguyen, K.-K. Lee, S. Hong, C.-H. Han, M. Cho, H.-K. Choi and K. Kwak, *Nano Energy*, 2021, **82**, 105721.
11. Y. Zhou, F. Fan, Y. Liu, S. Zhao, Q. Xu, S. Wang, D. Luo and Y. Long, *Nano Energy*, 2021, **90**, 106613.
12. H. Chen, D. Cho, K. Ko, C. Qin, M. P. Kim, H. Zhang, J.-H. Lee, E. Kim, D. Park, X. Shen, J. Yang, H. Ko, J.-W. Hong, J.-K. Kim and S. Jeon, *ACS Nano*, 2022, **16**, 68-77.
13. X. Yin, R. Yang, G. Tan and S. Fan, *Science*, 2020, **370**, 786-791.
14. A. P. Raman, M. A. Anoma, L. Zhu, E. Rephaeli and S. Fan, *Nature*, 2014, **515**, 540.
15. S. Wang, T. Jiang, Y. Meng, R. Yang, G. Tan and Y. Long, *Science*, 2021, **374**, 1501-1504.
16. K. Tang, K. Dong, J. Li, M. P. Gordon, F. G. Reichertz, H. Kim, Y. Rho, Q. Wang, C.-Y. Lin, C. P. Grigoropoulos, A. Javey, J. J. Urban, J. Yao, R. Levinson and J. Wu, *Science*, 2021, **374**, 1504-1509.
17. C. Lin, J. Hur, C. Y. H. Chao, G. Liu, S. Yao, W. Li and B. Huang, *Sci. Adv.*, 2022, **8**, eabn7359.
18. Y. Rao, J. Dai, C. Sui, Y.-T. Lai, Z. Li, H. Fang, X. Li, W. Li and P.-C. Hsu, *ACS Energy Letters*, 2021, **6**, 3906-3915.
19. Z. Zhou, Y. Fang, X. Wang, E. Yang, R. Liu, X. Zhou, Z. Huang, H. Yin, J. Zhou and B. Hu, *Nano Energy*, 2022, **93**, 106865.
20. S. Wang, Y. Zhou, T. Jiang, R. Yang, G. Tan and Y. Long, *Nano Energy*, 2021, **89**, 106440.
21. Y. Y. Cui, Y. Ke, C. Liu, N. Wang, Z. Chen, L. M. Zhang, Y. Zhou, S. Wang, Y. F. Gao and Y. Long, *Joule*, 2018, **2**, 1707-1746.
22. Y.-X. Ji, S.-Y. Li, G. A. Niklasson and C. G. Granqvist, *Thin Solid Films*, 2014, **562**, 568-573.
23. T. Chang, X. Cao, N. Li, S. Long, Y. Zhu, J. Huang, H. Luo and P. Jin, *Matter*, 2019, **1**, 734-744.
24. C. Cao, B. Hu, G. Tu, X. Ji, Z. Li, F. Xu, T. Chang, P. Jin and X. Cao, *ACS Appl. Mater. Interfaces*, 2022, **14**, 28105-28113.
25. X. Zhou, Y. Meng, T. D. Vu, D. Gu, Y. Jiang, Q. Mu, Y. Li, B. Yao, Z. Dong, Q. Liu and Y. Long, *J. Mater. Chem. A*, 2021, **9**, 15618-15628.
26. Y. Yu, P. Yi, W. Xu, X. Sun, G. Deng, X. Liu, J. Shui and R. Yu, *Nano-Micro Letters*, 2022, **14**, 77.
27. Z. Han, P. Wang, Y. Lu, Z. Jia, S. Qu and W. Yang, *Sci. Adv.*, 2022, **8**, eabl5066.
28. S. Zhang, S. Cao, T. Zhang, Q. Yao, A. Fisher and J. Y. Lee, *Mater. Horiz.*, 2018, **5**, 291-297.
29. G. Cai, J. Chen, J. Xiong, A. Lee-Sie Eh, J. Wang, M. Higuchi and P. S. Lee, *ACS Energy Letters*, 2020, **5**, 1159-1166.
30. H. Fu, X. Hong, A. Wan, J. D. Batteas and D. E. Bergbreiter, *ACS Appl. Mater. Interfaces*, 2010, **2**, 452-458.
31. T. Munk, S. Baldursdottir, S. Hietala, T. Rades, M. Nuopponen, K. Kalliomäki, H. Tenhu, J. Rantanen and C. J. Strachan, *Polymer*, 2013, **54**, 6947-6953.
32. X.-H. Li, C. Liu, S.-P. Feng and N. X. Fang, *Joule*, 2019, **3**, 290-302.
33. Y. Ke, Y. Yin, Q. Zhang, Y. Tan, P. Hu, S. Wang, Y. Tang, Y. Zhou, X. Wen, S. Wu, T. J. White, J. Yin, J. Peng, Q. Xiong, D. Zhao and Y. Long, *Joule*, 2019, **3**, 858-871.
34. Y. Tang, G. Lin, S. Yang, Y. K. Yi, R. D. Kamien and J. Yin, *Adv. Mater.*, 2017, **29**, 1604262.
35. T. C. Shyu, P. F. Damasceno, P. M. Dodd, A. Lamoureux, L. Xu, M. Shlian, M. Shtein, S. C. Glotzer and N. A. Kotov, *Nat. Mater.*, 2015, **14**, 785-789.

36. ANSI/ASHRAE/IES, *Energy standard for building except low-rise residential buildings*, 2019.
37. X. Sui, H. Guo, C. Cai, Q. Li, C. Wen, X. Zhang, X. Wang, J. Yang and L. Zhang, *Chemical Engineering Journal*, 2021, **419**, 129478.
38. J. Wu, Z. Wu, H. Xu, Q. Wu, C. Liu, B.-R. Yang, X. Gui, X. Xie, K. Tao, Y. Shen, J. Miao and L. K. Norford, *Mater. Horiz.*, 2019, **6**, 595-603.
39. J. Wu, Z. Wu, S. Han, B.-R. Yang, X. Gui, K. Tao, C. Liu, J. Miao and L. K. Norford, *ACS Appl. Mater. Interfaces*, 2019, **11**, 2364-2373.
40. Y. Wei, H. Wang, Q. Ding, Z. Wu, H. Zhang, K. Tao, X. Xie and J. Wu, *Mater. Horiz.*, 2022, **9**, 1921-1934.
41. Y. Bai, B. Chen, F. Xiang, J. Zhou, H. Wang and Z. Suo, *Appl. Phys. Lett.*, 2014, **105**, 151903.
42. Y. Zhou, C. Wan, Y. Yang, H. Yang, S. Wang, Z. Dai, K. Ji, H. Jiang, X. Chen and Y. Long, *Adv. Funct. Mater.*, 2019, **29**, 1806220.
43. G. Li, J. Chen, Z. Yan, S. Wang, Y. Ke, W. Luo, H. Ma, J. Guan and Y. Long, *Mater. Horiz.*, 2023, DOI: 10.1039/D3MH00057E.
44. H. Hu, S. Wang, S. Wang, G. Liu, T. Cao and Y. Long, *Adv. Funct. Mater.*, 2019, **29**, 1902922.
45. Y. Feng, S. Wang, Y. Li, W. Ma, G. Zhang, M. Yang, H. Li, Y. Yang and Y. Long, *Adv. Funct. Mater.*, 2023, **n/a**, 2211027.
46. Y. Ke, Q. Zhang, T. Wang, S. Wang, N. Li, G. Lin, X. Liu, Z. Dai, J. Yan, J. Yin, S. Magdassi, D. Zhao and Y. Long, *Nano Energy*, 2020, **73**, 104785.
47. G. Wyszecki and W. S. Stiles, *Color Science: Concepts and Methods, Quantitative Data and Fomulae*, Wiley, New York, Second Edition edn., 2000.
48. ASTM, *ASTM G173 Standard tables of reference solar spectral irradiances: direct normal and hemispherical on a 37 tilted surface*, American Society for Testing and Materials, Philadelphia, PA, USA, 2012.
49. Y. Ke, Y. Li, L. Wu, S. Wang, R. Yang, J. Yin, G. Tan and Y. Long, *ACS Energy Letters*, 2022, **7**, 1758-1763.
50. ANSI/ASHRAE/IES, *Energy standard for building except low-rise residential buildings*, 2016.

Supporting information for "Solar/Radiative Cooling Dual-Regulation Smart Window Based on Shape-morphing Kirigami Structures"

Shancheng Wang,[a,b‡] Yuting Dong,[b,‡] Yanbin Li,[c,‡] Keunhyuk Ryu,[b] Zhili Dong,[b] Jian Chen,[d] Zhendong Dai,[d] Yujie Ke,[e,*] Jie Yin,[c,*] and Yi Long[a,b,*]

[a]Department of Electrical Engineering, The Chinese University of Hong Kong, Shatin, New Territories, Hong Kong SAR, China

[b]School of Materials Science and Engineering, Nanyang Technological University, 639798 Singapore

[c]Department of Mechanical and Aerospace Engineering, North Carolina State University, Raleigh, North Carolina 27695, United States

[d]Jiangsu Provincial Key Laboratory of Bionic Functional Materials, College of Mechanical and Electrical Engineering, Nanjing University of Aeronautics and Astronautics, Nanjing 210016, China

[e]Institute of Materials Research and Engineering (IMRE), Agency for Science, Technology and Research (A*STAR), 2 Fusionopolis Way, Innovis #08-03, Singapore 138634, Republic of Singapore

[‡]These authors contributed equally to this work.

Email: yilong@cuhk.edu.hk; jyin8@ncsu.edu; yujie_ke@imre.a-star.edu.sg

Experiment and method

Materials

N-isopropylacrylamide (NIPAm, 98%, Wako Pure Chemical Industries Ltd), ammonium persulfate (APS, 98%, Sigma-Aldrich), N,N,N',N'-tetramethylethylenediamine (TEMED, 99%, Sigma-Aldrich), acrylamide (AAm, 98%, Sigma-Aldrich), N,N-methylenebis(acrylamide) (Bis, 99%, Sigma-Aldrich), 2-hydroxy-4'-(2-hydroxyethoxy)-2-methylpropiophenone, (98%, Sigma-Aldrich), benzophenone (99%, Sigma-Aldrich), methanol (99.8%, Sigma-Aldrich), acetone (99.8%, Fisher Chemical), glycerol (99.5%, Sigma-Aldrich), polyvinylpyrrolidone (PVP, average $Mw \approx 40000$, Sigma-Aldrich), sodium chloride (NaCl, 99%, Sigma-Aldrich), silver nitrate (99%, Sigma-Aldrich), ethanol (99.8%, Fisher Chemical) and SYLGARD™ 184 silicone elastomer kit of polydimethylsiloxane (PDMS, Dow Corning) were used without further purification. Deionized water (DI water) was used throughout the experiments.

Preparation of physically crosslinked smart PNIPAm hydrogel

The preparation of physically crosslinked PNIPAm follows the method reported in the literature.[43] 2.2625 g (0.02 mol) of NIPAm was dissolved in 23 ml of DI water at 25 °C by stirring in an atmosphere of argon to remove solved oxygen. Two aqueous solutions were prepared by dissolving 13.69 mg (0.06 mmol) of APS (initiator) in 1 ml of DI water and 27 µl (0.18 mmol) of TEMED (accelerator) with 1 ml of DI water, followed by mixing with the NIPAm solution at 300 rpm for 30 min to form 25 ml of homogenous solution. Then the solution was left for reaction for 24 h at room temperature. Finally, acetone was added to the solution to precipitate PNIPAm, and the obtained PNIPAm was dried in a vacuum oven at 60 °C.

Preparation of monomer ink for lamination

Monomer ink with 5wt%, 10wt%, 15wt%, and 20wt% PNIPAm concentrations was prepared. Respectively, 0.5 g, 1 g, 1.5 g and 2 g of the pure PNIPAm hydrogel was dissolved in 10 ml DI of water, followed by adding 2 g of AAm and stirring for 30 min. Then, 0.02 g of Bis and 0.1 g of 2-hydroxy-4'-(2-hydroxyethoxy)-2-methylpropiophenone (light initiator) was added and the mixture was stirred well. The monomer ink was prepared for lamination in later step.

Synthesis of AgNWs

The AgNWs were prepared according to the literature.[44] 1.76 g of polyvinylpyrrolidone (PVP) was added to 57 ml of glycerol. The mixture was stirred at 500 rpm for 2 h at 110 °C to form a homogenous solution and was then cooled down to room temperature. Next, 0.474 g of silver nitrate was added to the solution followed by a NaCl solution prepared by dissolving 17.7 mg of NaCl in 0.15 ml of DI water and 3 ml of glycerol. Subsequently, the mixture was heated to 210 °C from room temperature within 30 min under 200 rpm stirring, and heating was stopped when the temperature reached 210 °C. When the mixture cooled down to 100 °C, 60 ml of DI water was added, followed by subsequent cooling to room temperature. The obtained solution was kept undisturbed for one week before the collection of the sediment at the flask bottom. The obtained AgNWs were washed with ethanol thoroughly by centrifuging at 5000 rpm 3 times.

Preparation of PDMS film for the PDMS-composite hydrogel-PDMS sandwich structure

Firstly, the precursor and curing agent of PDMS gel were well mixed at a weight ratio of 10:1, followed by vacuum degassing to remove the bubbles. 2.5 g of the mixture was loaded on a plastic petri dish cover (d=9.5 cm) and spin-coated at 1000 rpm for 30 s. The PDMS was then cured in an oven at 60 °C for ~2 h. The obtained thin PDMS films were cut into the size of 5×5 cm for the subsequent lamination process.

Lamination of the PDMS-composite hydrogel-PDMS sandwich structure

There were three steps for the lamination process, namely (1) pre-treatment of PDMS film, (2) sealing, and (3) crosslinking. (1) For the pre-treatment step, two pieces of PDMS thin films were immersed in a benzophenone solution (20wt% in acetone) to facilitate chemical bonds between PDMS and PNIPAm for 15 min. Then, the thin films were rinsed with methanol and dried in a vacuum desiccator. (2) For the subsequent sealing process, one piece of benzophenone immersed PDMS film was transferred to a glass substrate and covered by a mould with a 5 cm × 5 cm × 1 mm square hole. The monomer ink was then poured into the hole of the mould. And another benzophenone immersed PDMS film was placed onto the mould to cover the uncrosslinked monomer ink. The side of structure was then sealed with epoxy. (3) Finally, for the crosslinking step, the sealed sandwich structure was exposed under 365 nm UV for 5 min for the hydrogel to fully crosslink.

Spin coating of AgNWs

Prepared AgNWs were dispersed in ethanol and ultrasonicated to form a suspension of ~5 mg/ml. The fabricated sandwich structure was pre-strained to 40% and treated by O_2 plasma for 1 min. Then, 0.75 ml of the AgNWs suspension was spin-coated at 1000 rpm for 30 s. The coating process was conducted 1, 5, 10, and 15 times for the samples with 1, 5, 10, and 15 layers of AgNWs.

Preparation of PDMS films for kirigami structure

2.5 g of PDMS precursor and 0.25 g of PDMS curing agent were mixed with 2.75 g of hexane. The mixture was transferred to a plastic petri dish (d=9.5 cm). The hexane was removed by ~1 h evaporation at room temperature in a fume hood. Then, the stiff mixture was cured in an oven under 60 °C for ~2 h to make thick PDMS films.

Preparation of reconfigurable kirigami structure

The designed kirigami patterns were printed on paper and cut manually to get the paper kirigami structures. The PDMS kirigami structures were cut manually using the printed kirigami pattern as a template.

Morphological characterization of smart hydrogel and the AgNWs

The SEM images of smart hydrogel and AgNWs were taken with SEM Supra 55 (Carl Zeiss). To obtain the microstructure of hydrogels below and above LCST (20 °C), the two samples of smart hydrogel were placed at 15 and 45 °C separately for 1 h. Then the two samples were immediately submerged in liquid nitrogen until fully frozen. Due to the extremely low temperature of liquid nitrogen, the microstructures of the hydrogel at different temperatures were preserved.[45] The frozen hydrogels were placed into a freeze-dryer for the freeze-drying process for 72 h. The freeze-dried aerogels were subsequently used to take the SEM images.

The AgNWs were coated onto PDMS substrate and the SEM images for the released and stretched states were captured.

Rheological characterization of smart hydrogel samples

The rheological properties of the composite hydrogel inks with 5%, 10%, 15% and 20% PNIPAm concentration were measured by Anton Paar MCR 702e rheometer with a cone and plate geometry at a reference temperature of 15 °C. Hydrogel with a thickness of 0.5 mm and diameter of 15 mm was prepared. The storage modulus (G') and loss modulus (G'') were measured at a constant oscillatory shear strain of 0.5% with angular frequency ranging from 100 rad/s to 0.1 rad/s. The viscosity was measured with shear rates ranging from 0.01 to 100 s^{-1}.

Optical characterization of smart hydrogel, AgNWs, kirigami structures, and smart window

A UV-Vis spectrometer system (AvaSpec-ULS2048L StarLine Versatile Fiber-optic Spectrometer and AvaSpec-NIR256-2.5-HSC-EVO, Avantes) with a heating/cooling stage (PE120, Linkam) equipped was employed to collect the UV-Vis-NIR transmittance and reflectance spectra. The luminous transmittance (T_{lum}, 360-780 nm), IR transmittance ($T_{IR,}$ 780-2500 nm), and solar transmittance (T_{sol}, 250-2500 nm) were calculated by Equation 1:[46]

$$T_{lum/IR/sol} = \int \varphi_{lum/sol} T(\lambda) d\lambda \Big/ \int \varphi_{lum/sol} d\lambda \quad (1)$$

In this formula $T(\lambda)$ is spectral transmittance, $\psi_{lum}(\lambda)$ is the standard luminous efficiency function of photopic vision in the wavelength range of 360–780 nm[47]. On the other hand, $\psi_{sol}(\lambda)$ is the solar irradiance spectrum for air mass 1.5 (corresponding to the sun standing 37° above the horizon with 1.5-atmosphere thickness, which corresponds to a solar zenith angle of 48.2°)[48]. The solar modulation ability ΔT_{sol} was calculated with Equation 2:

$$\Delta T_{\mathrm{NIR/sol}} = T_{\mathrm{NIR/sol,20℃}} - T_{\mathrm{NIR/sol,90℃}} \quad (2)$$

The reflectance R_{lum} and R_{sol} were calculated using Equation 3:

$$R_{\mathrm{lum/sol}} = \int \varphi_{\mathrm{lum/sol}} R(\lambda) d\lambda \Big/ \int \varphi_{\mathrm{lum/sol}} d\lambda \quad (3)$$

Where $R(\lambda)$ is the spectral reflectance (360-780 nm for R_{lum} and 250-2500 nm for R_{sol}). $\psi_{lum}(\lambda)$ is the standard luminous efficiency function of photopic vision for the wavelength of 360–780 nm while $\psi_{sol}(\lambda)$ is the solar irradiance spectra for air mass 1.5, respectively.

Emissivity measurement of AgNWs and smart window

The emissivity curve was plotted according to Kirchhoff's law of thermal radiation: $\varepsilon(\lambda) = A(\lambda) = 1\text{-}T(\lambda)\text{-}R(\lambda)$.[49] $R(\lambda)$ and $T(\lambda)$ are the spectral reflectance and the spectral transmittance that was measured by FTIR spectrometer (Perkin Elmer Frontier) with an integration sphere attached. The integrated broadband emissivity were calculated with Equation 4:[49]

$$\varepsilon_{\mathrm{Broadband}} = \frac{\int_{2.5\ \mu m}^{20\ \mu m} I_{BB}(T,\lambda)\varepsilon(T,\lambda)\, d\lambda}{\int_{2.5\ \mu m}^{20\ \mu m} I_{BB}(T,\lambda) d\lambda} \quad (4)$$

$I_{BB}(T, \lambda)$ is the spectral intensity emitted by a blackbody at temperature T and $\varepsilon(T, \lambda)$ is the surface's spectral hemispherical thermal emittance for the wavelength of 2.5-20 μm.

Mechanical characterization of the smart hydrogel and kirigami samples

The mechanical properties of smart hydrogel and paper kirigami were tested by Instron 5567 mechanical tester with tensile extension mode. Rectangular hydrogel samples with a thickness of 0.5 mm were prepared for the mechanical test. For PDMS kirigami samples, MTS Mechanical Tester Model 42 was used to measure the mechanical properties.

Numerical performance evaluation of the reconfigurable kirigami structure

Two performance indices namely length ratio and covering ratio were defined to quantitatively evaluate the performance of reconfigurable kirigami designs with different asymmetric ratios. The length ratio is defined as the ratio of the lengths of the two sides of the opening labelled as L_1 and L_2, which characterizes the degree of asymmetry for the stretched kirigami structure. The covering ratio is defined as the ratio of the exposed area (A_1) to the total area (A_2) of the out-of-plane kirigami, reflecting the ability of the kirigami structure to expose underlying layers upon stretching.

Mechanical simulation of the reconfigurable kirigami structure

The mechanical simulation of the kirigami structure was conducted with commercial FEM software ABAQUS. Three 5×5 structures are simulated with the asymmetric ratio as 1, 1.5, 3, 5, and 10 separately. The cut widths of all three structures were set as 2 mm and the cut corner was set as a circle-shape with a radius of 1.25 mm to reduce stress concentration. All three different structures were simulated as a three-dimensional problem. Given the experimentally fabricated PDMS (10:1) material, the neo-Hookean energy model was used here with shear modulus as 2 MPa and Poisson's ratio as 0.495 to approximate the incompressibility of hyper-elastic PDMS materials. The C3D8R element type was utilized for mesh. For loading conditions, the top cross-section of the model was totally constrained and only the bottom surface was uniaxially stretched.

Durability measurement of the smart window

The durability measurements with different environmental temperatures were conducted with laminated smart hydrogel and conventional PNIPAm hydrogel. The measurements were conducted with two environment setups: room temperature (25 °C, 10%RH) and high temperature (60 °C, 10%RH). The transmittance at 650 nm at 15 and 45 °C for all samples was measured and the ΔT_{650nm} was calculated. The samples were considered as failed when their ΔT_{650nm} reduced to 0 and the exposure times were recorded as the lifetimes of the samples.

Cycle stability measurement of the smart window

The cycle stability of the smart window was evaluated by measuring its T_{650nm} at 15 and 45 °C after repeating heating/cooling cycles. T_{650nm} at different temperatures were recorded for the original state and every 5 cycles until 125 heating/cooling cycles.

Energy-saving performance simulation for the smart window and literature-reported cases

EnergyPlus was used in the energy consumption simulation. In this simulation, a building model with the dimensions of 8 m in length, 6 m in width, and 2.7 m in height was used. The floor area was 48 m^2 and the total external wall surface area of the building was 75.6 m^2. Four windows with the dimension of 3 m in width and 2 m in height were installed in the four orientations to avoid the impact of orientation. The window covered 31.7% of the total wall surface area. The structure of the model house is shown in figure S20. Hourly weather data for a Typical Meteorological Year (TMY) was employed as the external boundary conditions.[50] In this simulation, the energy usage based on the unit of MJ m^{-2} was calculated based on the floor area.

For the global average energy saving performance comparison, clear glass, durable solar/RC dual-control smart window, RCRT smart window,[15] and STR smart window[17] were used for this simulation. The optical data for clear glass and the smart window are listed in table S3 while the optical data for the rest were obtained from the respective literature. The energy savings of all samples were calculated with the climate data of Singapore; Hong Kong SAR, China; Melbourne, VIC, Australia; Paris, France; London, UK; and Juneau, AK, U.S. (figure S22). The energy-saving data were then averaged to obtain the global average energy-saving performance of different samples.

For the 24-hour room temperature simulation, the clear glass, conventional PNIPAm hydrogel, commercial low-E glass, and durable solar/RC dual-control smart window were employed with their optical data listed in table S3. In this simulation, the HVAC system was switched off. Climate data from Singapore; Hong Kong SAR, China; Paris, France; and Juneau, AK, U.S. were used in this simulation. The climate data for 15th January was used in the winter room temperature simulation, and the climate data for 15th July was used in the summer room temperature simulation. It is worth mentioning that due to its tropical climate, there is no winter season in Singapore. Therefore, the room temperature curves in January and July are similar for Singapore.

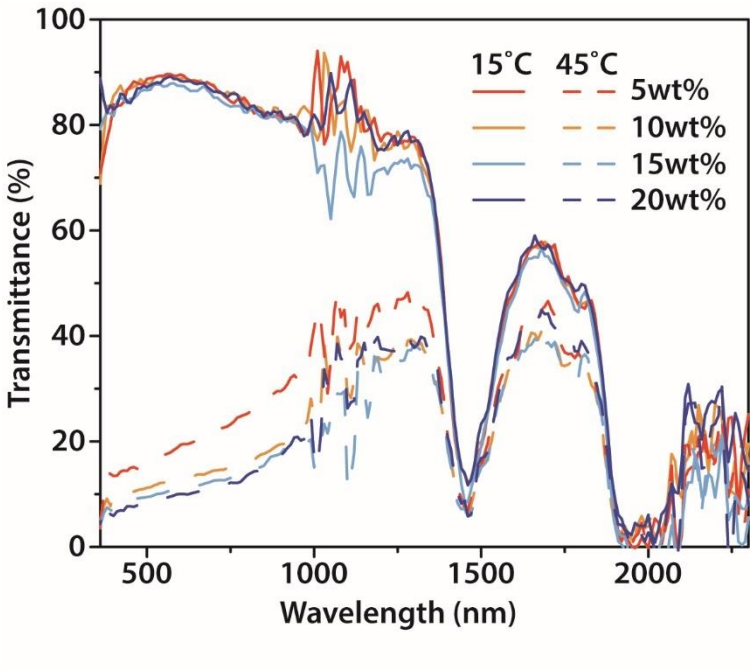

figure S1. UV-Vis spectra for smart hydrogels with different PNIPAm concentrations at 15 and 45 °C

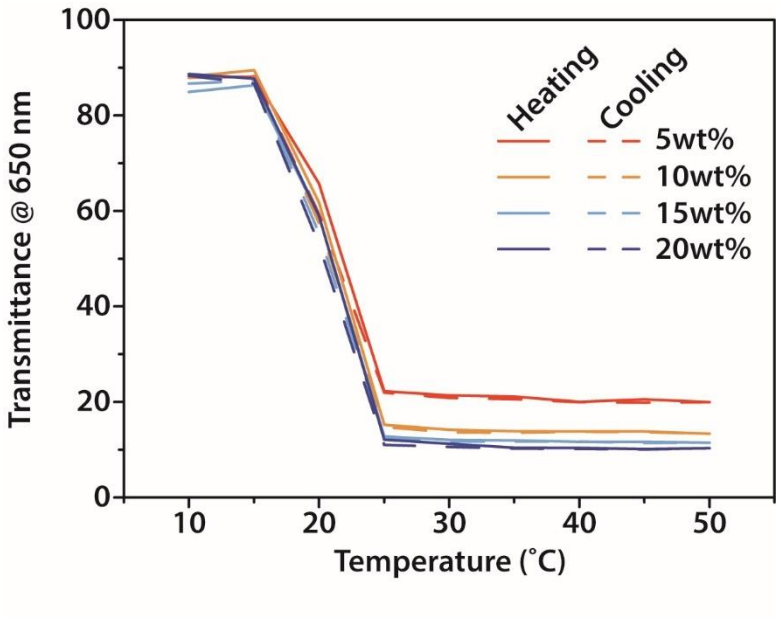

figure S2. Hysteresis loops for smart hydrogels with different PNIPAm concentrations.

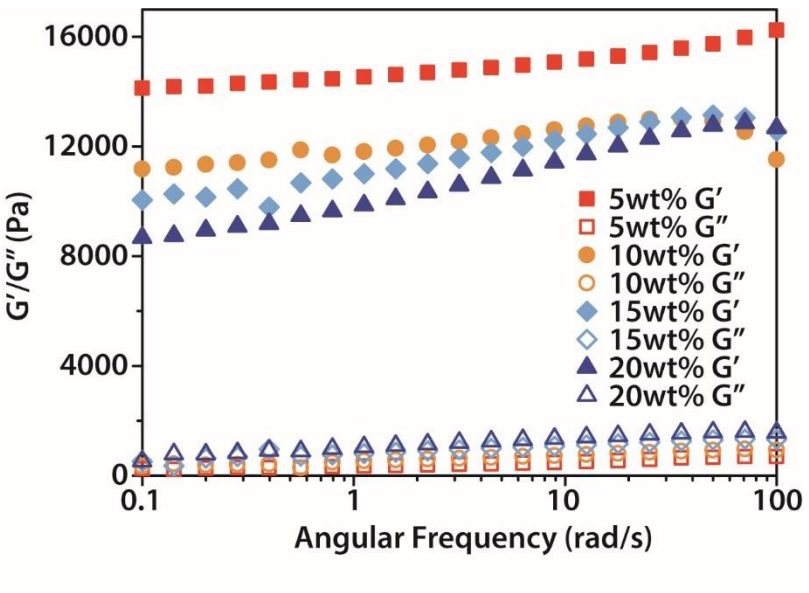

figure S3. G' and G" chart against angular frequency for the smart hydrogels with different PNIPAm concentrations.

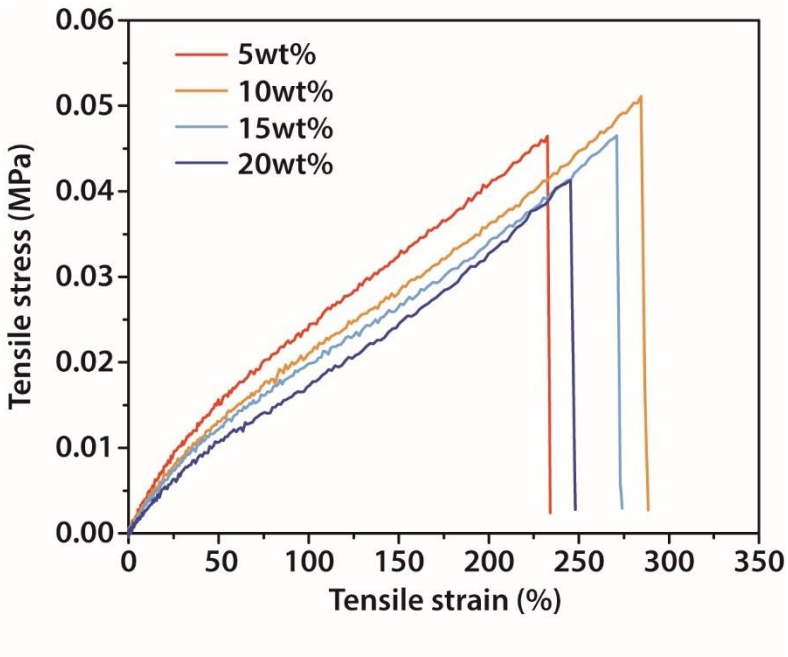

figure S4. Tensile curves for smart hydrogels with different PNIPAm concentrations.

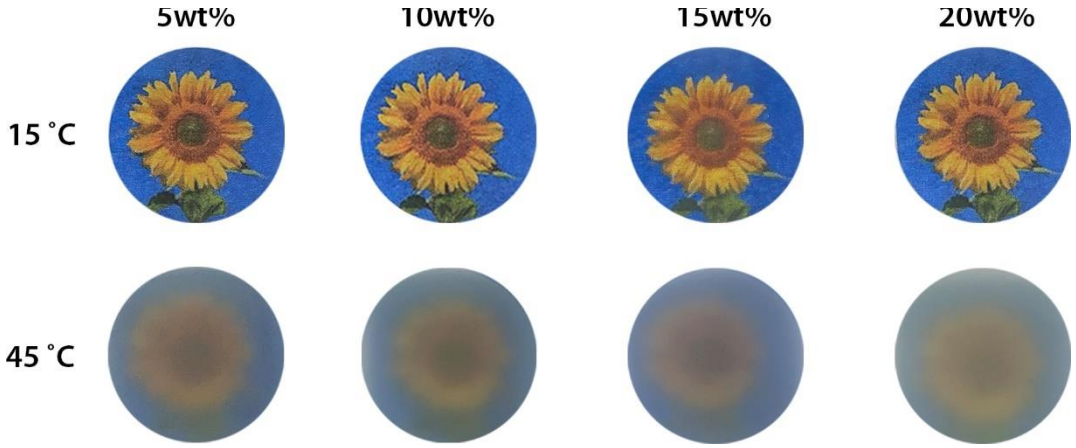

figure S5. Photos of smart hydrogels with different PNIPAm concentrations at 15 and 45 °C.

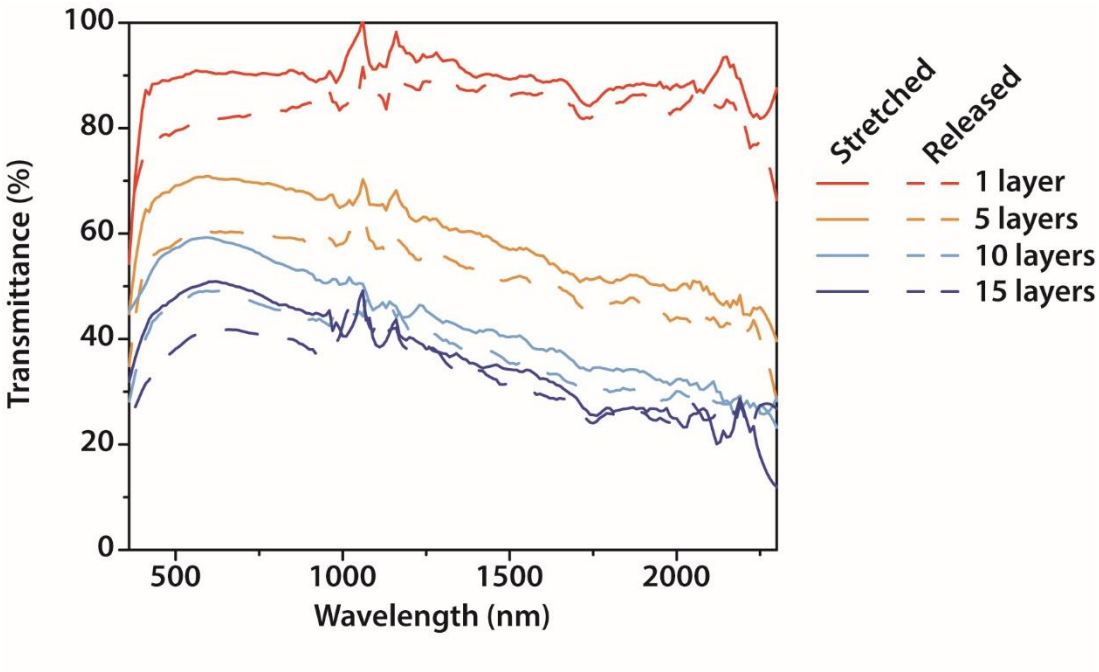

figure S6. UV-Vis spectra for different layers of AgNWs coated PDMS at stretched and released states.

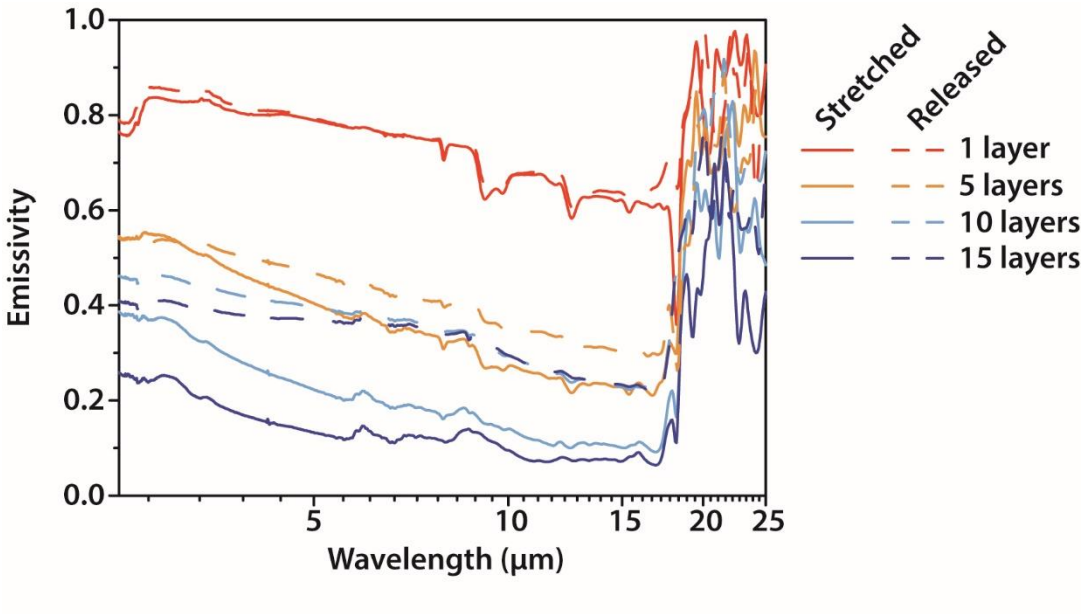

figure S7. Broadband emissivity spectra for different layers of AgNWs coated PDMS at stretched and released states.

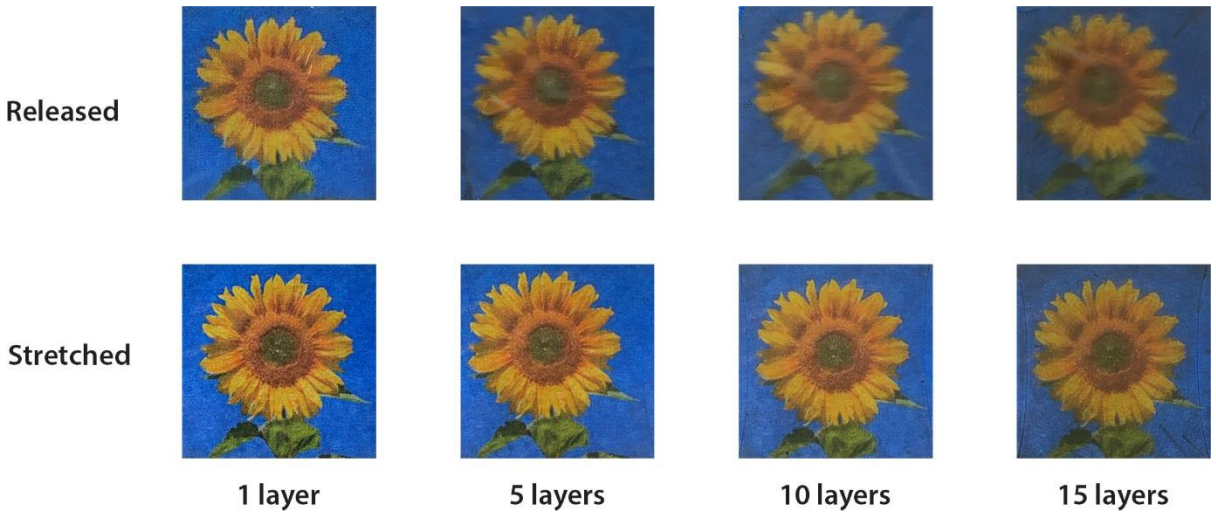

figure S8. Photos of different layers of AgNWs coated PDMS at stretched and released states.

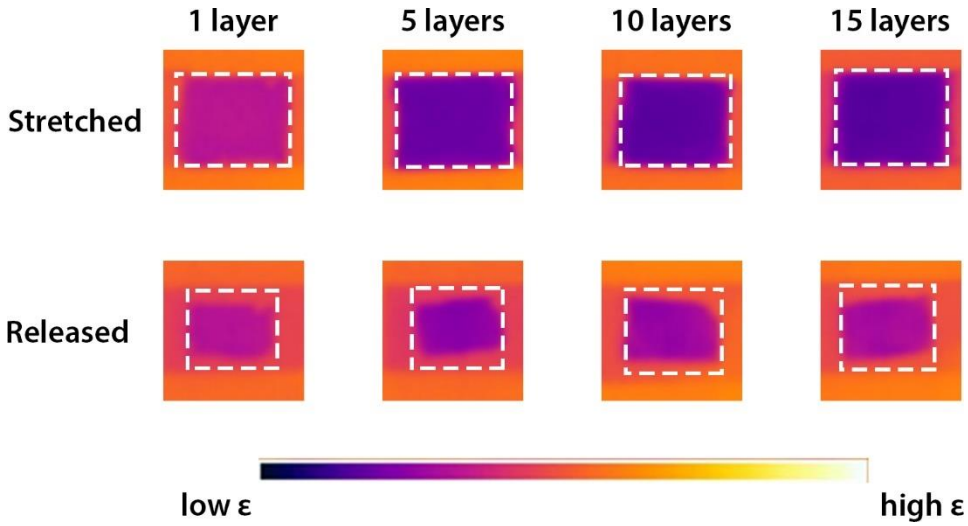

figure S9. IR camera images for different layers of AgNWs coated PDMS at stretched and released states. The samples are circled by dashed squares.

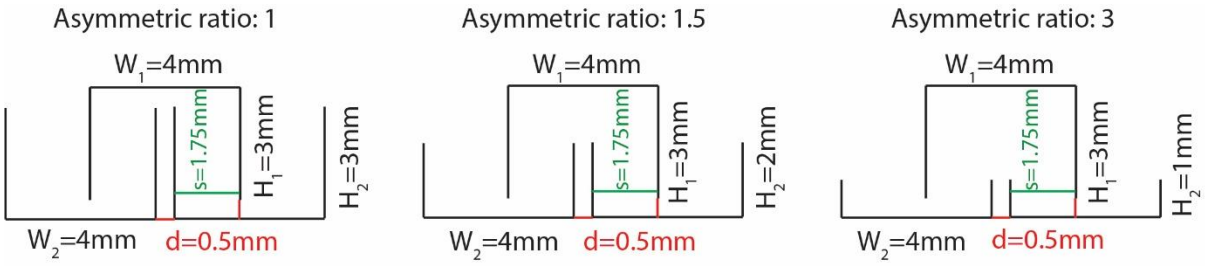

figure S10. Design of off-plain reconfigurable kirigami patterns with different geometric features.

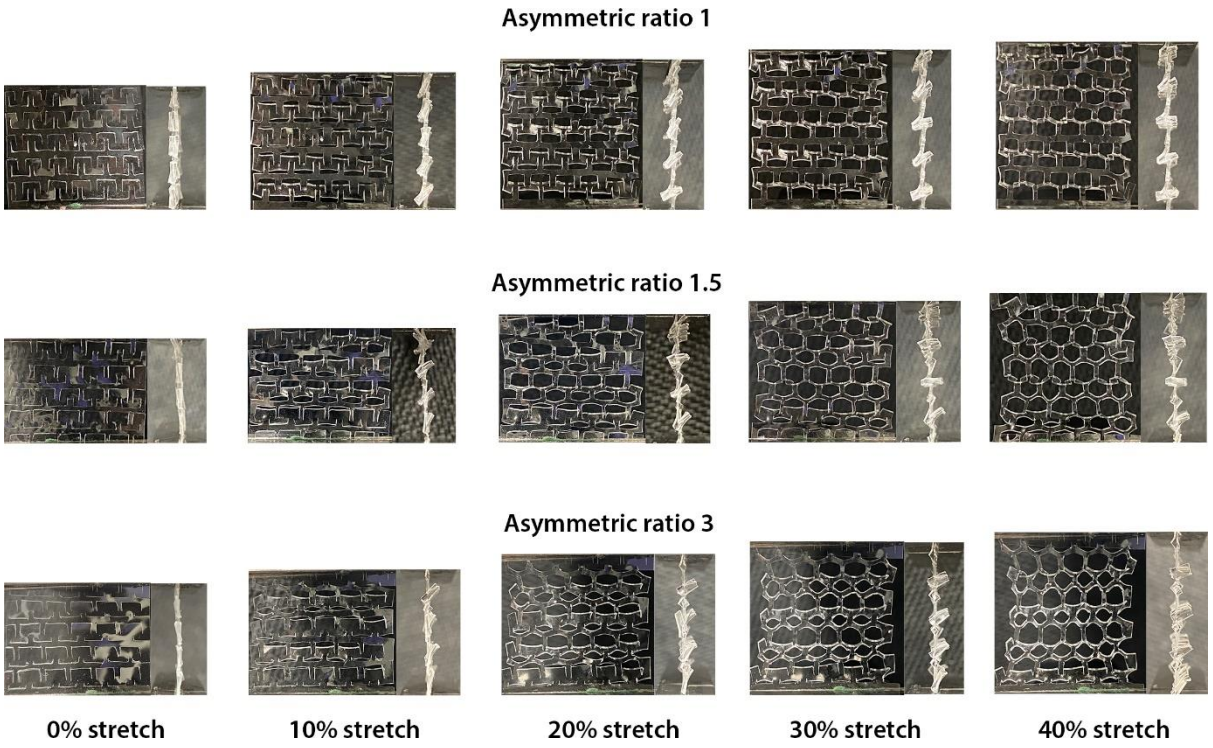

figure S11. Structure reconfiguration process for the kirigami structures with different asymmetric ratios.

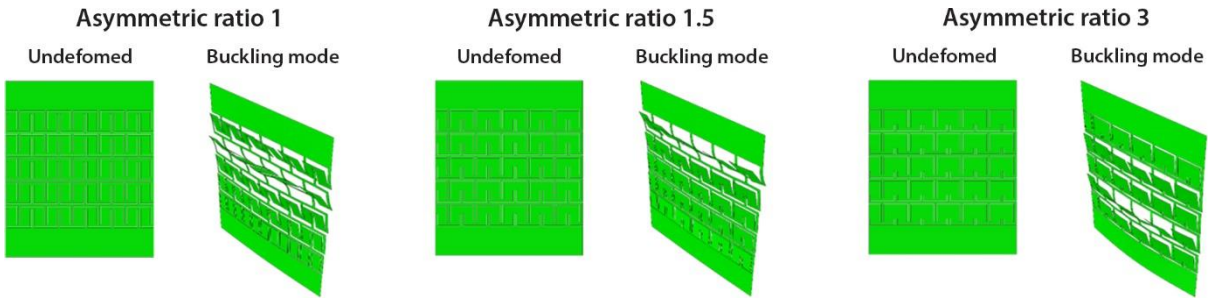

figure S12. FEM models of kirigami structures with different asymmetric ratios used for mechanical behaviour simulations.

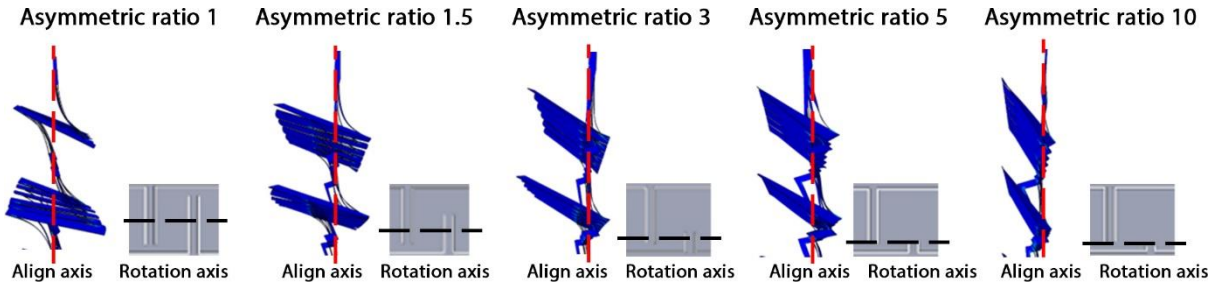

figure S13. Side views of the FEM simulated kirigami structures with different asymmetric ratios, their stretching direction, i.e., the aligning axis (red dashed line), and rotation axis (black dash line).

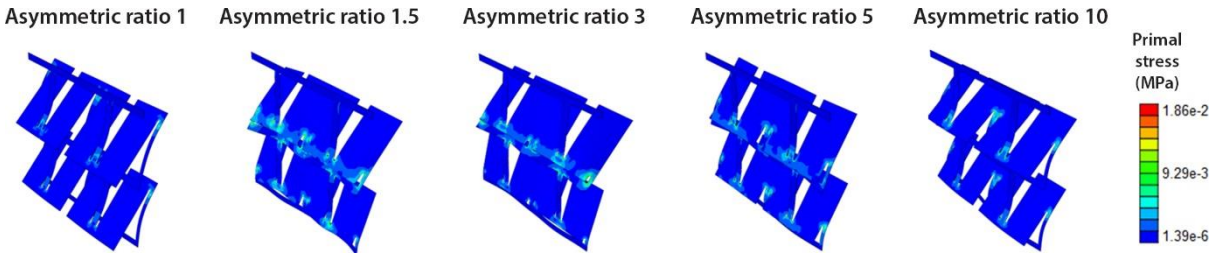

figure S14. Corner views of the primal stress distribution for the FEM simulated kirigami structures with different asymmetric ratios.

figure S15. Photos of out-of-plane kirigami structures with different PDMS thicknesses. The photos were taken with the 40% stretched samples.

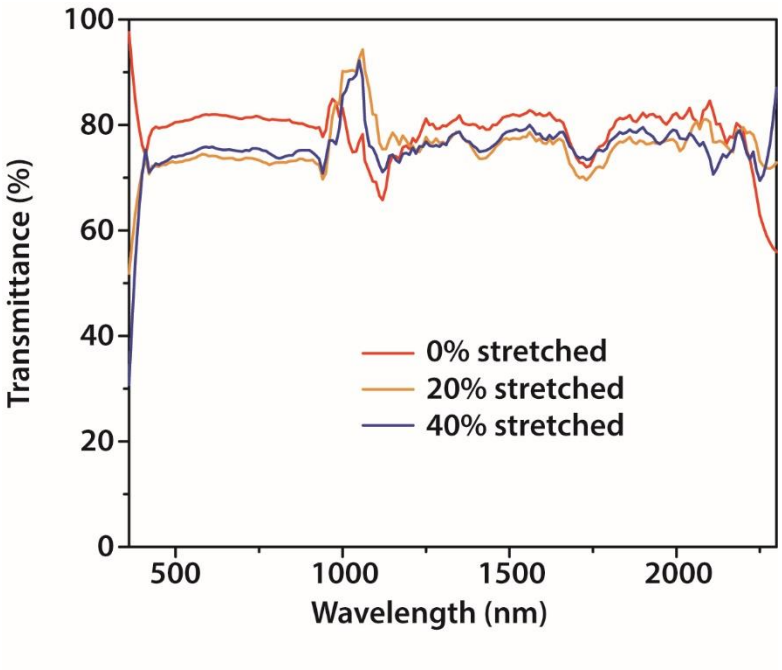

figure S16. UV-Vis spectra for the out-of-plane kirigami structure based on 0.3 mm PDMS under different strains.

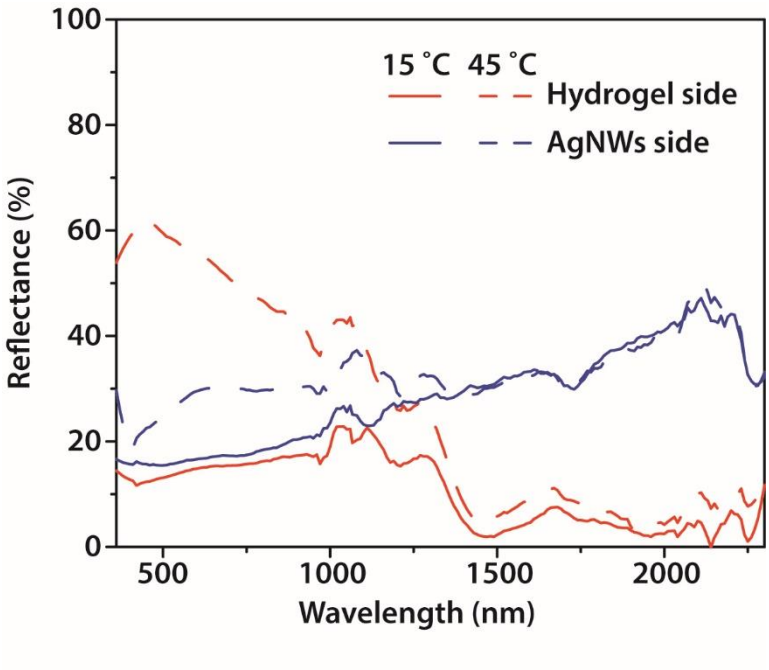

figure S17. Reflectance spectra for different sides of the durable solar/RC dual-control smart window at 15 and 45 °C.

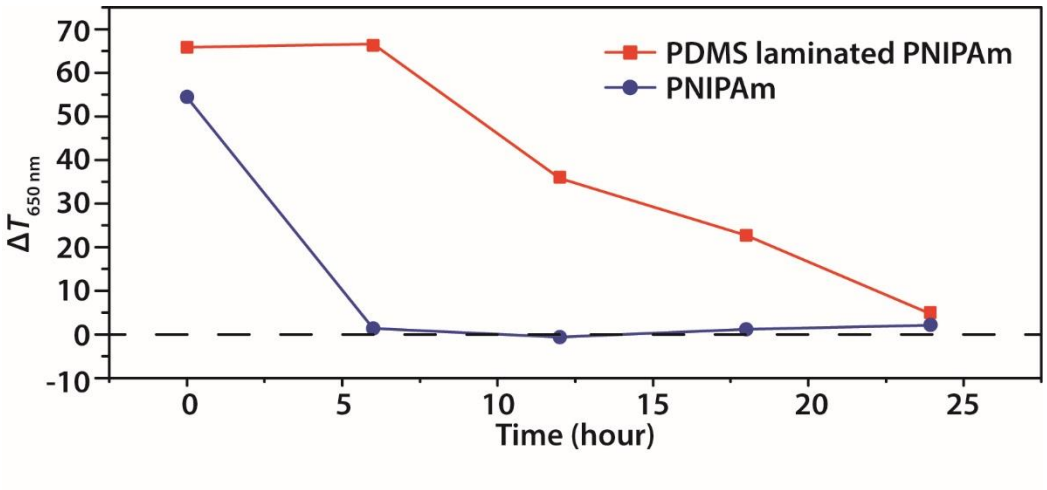

figure S18. High temperature (60 °C, 10%RH) durability test result for conventional PNIPAm and PDMS laminated PNIPAm.

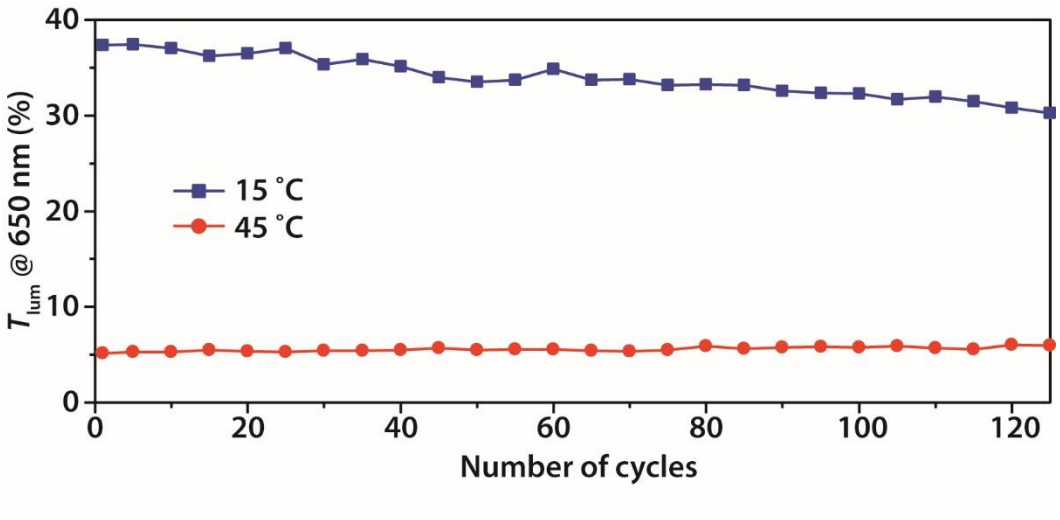

figure S19. Cycle stability for durable solar/RC dual-control smart window.

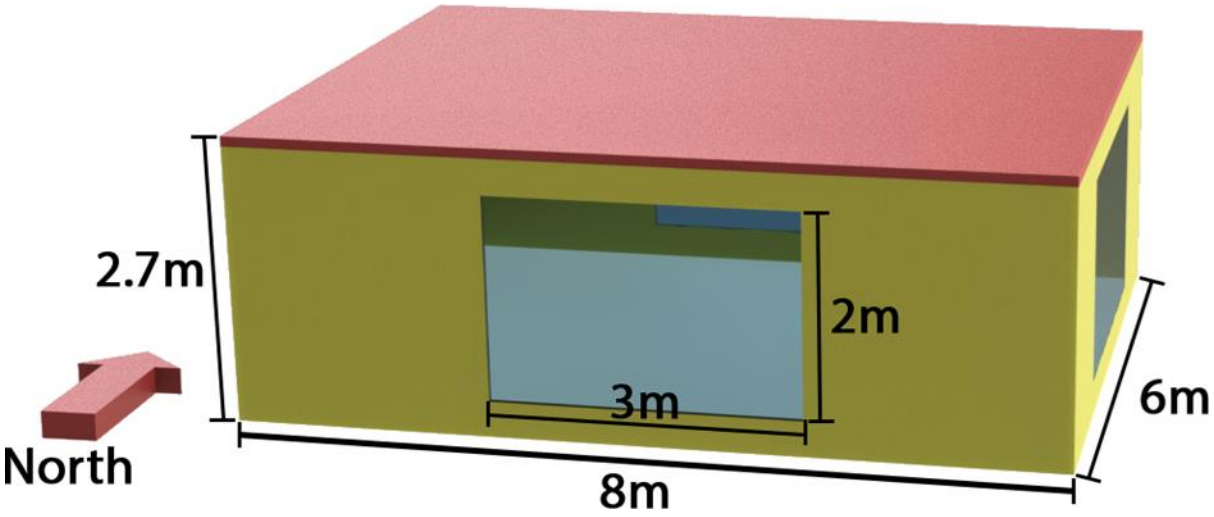

figure S20. Building model used for actual building energy consumption simulations and internal temperature simulations.

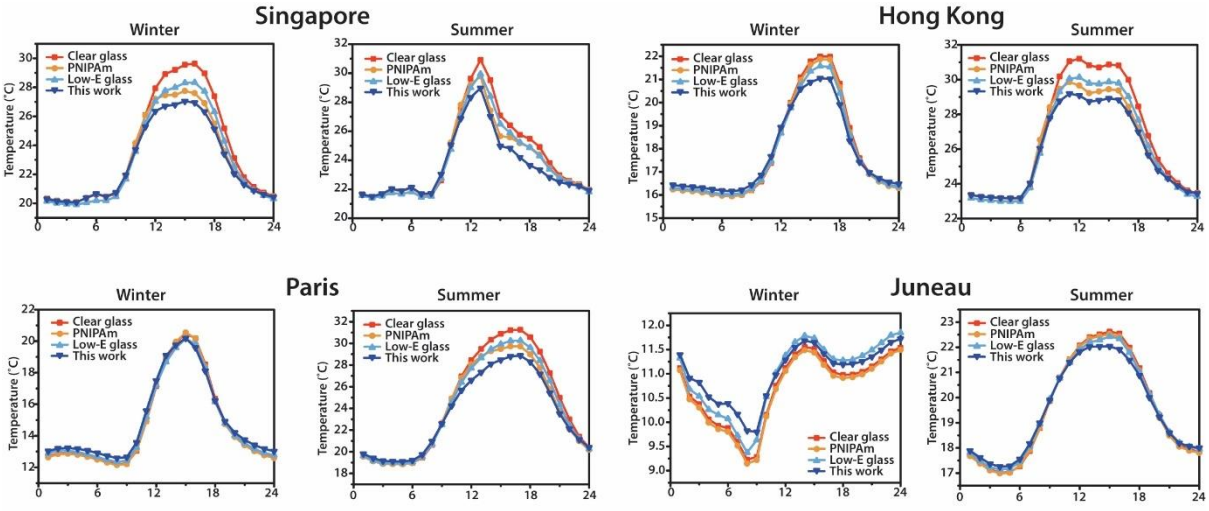

figure S21. 24-hour internal room temperature simulation results for clear glass, PNIPAm, low-E glass and durable solar/RC dual-control smart window in different climate regions and seasons. It should be noted that due to its tropical climate, there is no winter season in Singapore. Therefore, the room temperature curves for January and July are similar for Singapore.

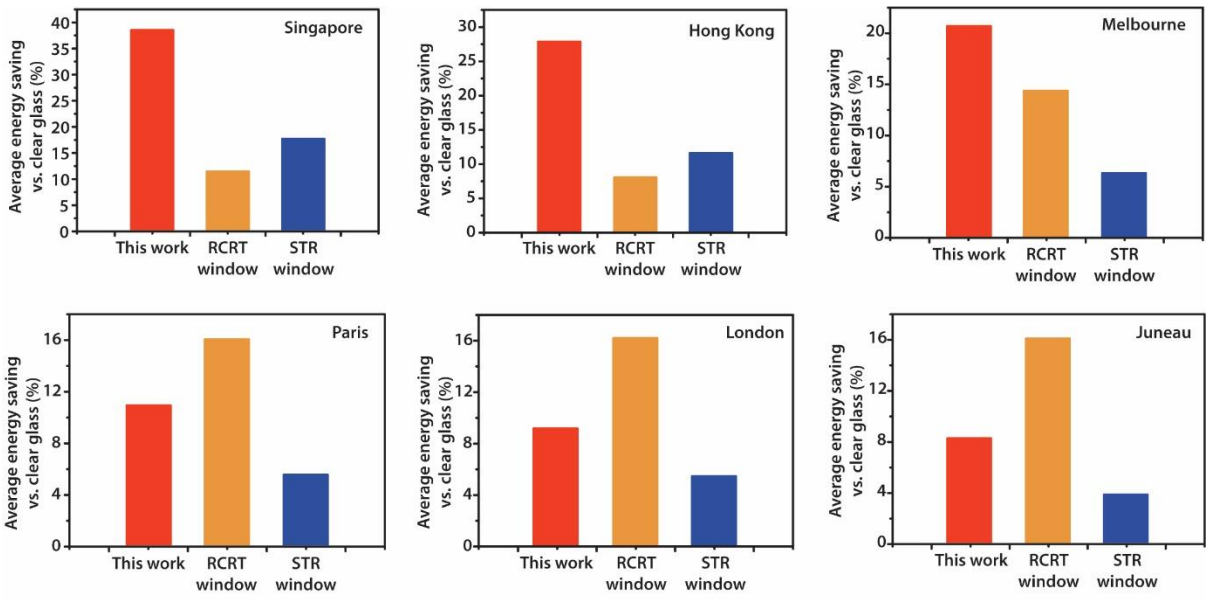

figure S22. Annual average energy saving performance for durable solar/RC dual-control smart window, RCRT smart window, and STR smart window in different cities. The clear glass was used as a baseline in this simulation.

table S1. Summary of optical properties for smart hydrogels and viscosities for monomer inks with different PNIPAm concentrations.

PNIPAm concentration	T_{lum} (%)	ΔT_{lum} (%)	ΔT_{sol} (%)	Viscosity (cP)
5wt%	89.2	76.6	54.1	115.8
10wt%	88.8	71.4	60.5	487.1
15wt%	87.3	76.9	60.3	1318.2
20wt%	88.3	79.0	62.3	2650.6

table S2. Summary of optical properties and Broadband emissivity for different layers of AgNWs coated PDMS.

AgNWs layer	T_{lum} (%)		T_{sol} (%)		$\varepsilon_{Broadband}$	
	Stretched	Released	Stretched	Released	Stretched	Released
1 layer	90.4	80.8	87.5	80.2	0.70	0.71
5 layers	70.2	59.8	64.5	55.7	0.36	0.42
10 layers	58.6	48.2	51.0	43.0	0.22	0.36
15 layers	49.8	43.3	40.5	37.2	0.16	0.34

table S3. Optical properties and Broadband emissivity for clear glass, PNIPAm hydrogel, commercial low-E glass, and durable solar/RC dual-control smart window used for energy simulation.

Simulation parameters	Clear glass	Conventional hydrogel	Commercial low-E glass	Durable solar/RC dual-control smart window
T_{lum} (%)	89.8	90.2 (20 °C) 5.5 (40 °C)	85	37.1 (15 °C) 6.7 (30 °C)
$R_{lum\text{-}Front}$ (%)	8.1	5.1 (20 °C) 26.9 (40 °C)	5.6	16.2 (15 °C) 27.7 (30 °C)
$R_{lum\text{-}Back}$(%)	8.1	5.1 (20 °C) 26.9 (40 °C)	7.9	14.2 (15 °C) 57.3 (30 °C)
T_{sol} (%)	83.7	66.8 (20 °C) 6.5 (40 °C)	63	30.6 (15 °C) 6.9 (30 °C)
$R_{sol\text{-}Front}$ (%)	7.5	5.9 (20 °C) 19.6 (40 °C)	19	19.8 (15 °C) 28.4 (30 °C)
$R_{sol\text{-}Back}$ (%)	7.5	5.9 (20 °C) 19.6 (40 °C)	22	14.1 (15 °C) 44.4 (30 °C)
$\varepsilon_{Broadband\text{-}Front}$	0.84	0.89	0.84	0.45 (15 °C) 0.95 (30 °C)
$\varepsilon_{Broadband\text{-}Back}$	0.84	0.89	0.1	0.95

video S1. FEM simulated structure reconfiguration animation for asymmetric ratio 1 kirigami structure.

video S2. FEM simulated structure reconfiguration animation for asymmetric ratio 1.5 kirigami structure.

video S3. FEM simulated structure reconfiguration animation for asymmetric ratio 3 kirigami structure.

video S4. FEM simulated structure reconfiguration animation for asymmetric ratio 5 kirigami structure.

video S5. FEM simulated structure reconfiguration animation for asymmetric ratio 10 kirigami structure.